Water mass analysis along 22 °N in the subtropical North Atlantic for the JC150 cruise (GEOTRACES, GApr08)

Lise Artigue, F. Lacan, Simon van Gennip, Maeve Lohan, Neil Wyatt, E. Malcolm S. Woodward, Claire Mahaffey, Joanne Hopkins, Yann Drillet

Water mass analysis along 22 °N in the subtropical North Atlantic for the JC150 cruise (GEOTRACES, GApr08)

Lise Artigue[1], François Lacan[1], Simon van Gennip[2], Maeve C. Lohan[3], Neil J. Wyatt[3], E. Malcolm S. Woodward[4], Claire Mahaffey[5], Joanne Hopkins[6] and Yann Drillet[2]

[1]LEGOS, University of Toulouse, CNRS, CNES, IRD, UPS, 31400 Toulouse, France.

[2]MERCATOR OCEAN INTERNATIONAL, Ramonville Saint-Agne, France.

[3]Ocean and Earth Science, University of Southampton, National Oceanographic Center, Southampton, UK SO14 3ZH.

[4]Plymouth Marine Laboratory, Plymouth, PL1 3DH. UK.

[5]Department of Earth, Ocean and Ecological Sciences, School of Environmental Sciences, 4 Brownlow Street, University of Liverpool, Liverpool, L69 3GP.

[6]National Oceanography Centre, Liverpool, L3 5DA, UK.

Corresponding author: Lise Artigue***** (lise.artigue@gmail.com),

***** LEGOS/CNES, 18, avenue Edouard Belin – 31401 Toulouse Cedex 9, France

Key words: Water mass; Optimum multiparameter analysis (OMPA); Lagrangian particle tracking experiment; subtropical North Atlantic; JC150; GEOTRACES

Funding Source:

- University of Toulouse public funding awarded to Lise Artigue
- French national research (CNRS) public funding awarded to François Lacan
- NERC with reference NE/N001979/1 awarded to Claire Mahaffey (University of Liverpool) and Malcolm Woodward (PML) and NE/N001125/1 awarded to Maeve Lohan (University of Southampton).
- Mercator Ocean International for Simon van Gennip and Yann Drillet.

Abstract

This study presents a water mass analysis along the JC150 section in the subtropical North Atlantic, based on hydrographic and nutrient data, by combining an extended optimum multiparameter analysis (eOMPA) with a Lagrangian particle tracking experiment (LPTE). This combination, which was proposed for the first time, aided in better constraining the eOMPA end-member choice and providing information about their trajectories. It also enabled tracing the water mass origins in surface layers, which cannot be achieved with an eOMPA. The surface layers were occupied by a shallow type of Eastern South Atlantic Central Water (ESACW) with traces of the Amazon plume in the west. Western North Atlantic Central Water dominates from 100–500 m, while the 13 °C-ESACW contribution occurs marginally deeper (500–900 m). At approximately 700 m, Antarctic Intermediate Water (AAIW) dominates the west of the Mid-Atlantic Ridge (MAR), while Mediterranean Water dominates the east with a small but non-negligible contribution down to 3500 m. Below AAIW, Upper Circumpolar Deep Water is observed throughout the section (900–1250 m). Labrador Sea Water (LSW) is found centered at 1500 m, where the LPTE highlights an eastern LSW route from the eastern North Atlantic to the eastern subtropical Atlantic, which was not previously reported. North East Atlantic Deep Water (encompassing a contribution of Iceland-Scotland Overflow Water) is centered at ~2500 m, while North West Atlantic Bottom Water (NWABW, encompassing a contribution of Denmark Strait Overflow Water) is principally localized in the west of the MAR in the range of 3500–5000 m. NWABW is also present in significant proportions (> 25 %) in the east of the MAR, suggesting a crossing of the MAR possibly through the Kane fracture zone. This feature has not been investigated so far. Finally, Antarctic Bottom Water is present in deep waters throughout the section, mainly in the west of the MAR.

Source waters have been characterized from GEOTRACES sections, which enables estimations of trace elements and isotope transport within water masses in the subtropical North Atlantic.

1 Introduction

Oceanic water masses store and transport considerable amounts of energy, water and chemical elements in the earth's surface. These water masses impact the atmosphere through interactions at the air/sea interface. Water mass analysis, which consist in studying the formation, spreading, and mixing of water masses, is therefore essential to understand the role of oceans in climate processes. The methods used for water mass analysis have evolved from classical descriptions of oceanic circulation based on hydrographic properties to the determination of water mass formation regions, transport pathways, and mixing length scales from numerical models and novel tracer data (Tomczak, 1999). An example of such development is the introduction of the optimum multiparameter analysis (OMPA, Tomczak, 1981). This method enables estimating the contributions of different water masses defined in specific locations (end-members) to a measured ocean section based on a range of hydrographic parameters. This method demonstrates a significant amount of improvement compared to previous methods and has been widely used (Álvarez et al., 2014; García-Ibáñez et al., 2018; Jenkins et al., 2015; Pardo et al., 2012; Peters et al., 2018). However, the results of OMPA are strongly dependent on the choice of water mass end-members that possibly impact the ocean section, and OMPA cannot provide any information related to surface layers. Moreover, a water mass analysis conducted only with OMPA does not provide direct information on the water mass pathways between their formation region and the measured section. Therefore, the water mass analysis proposed in this study combines, for the first time to the best of our knowledge, an extended OMPA with a Lagrangian particle tracking

experiment (LPTE) to better constrain the end-members and provide information on water mass pathways. LPTEs are widely used in recent times to investigate several aspects of ocean sciences, such as oceanic circulation (eg. Spence et al., 2014) or biogeochemistry (eg. Cetina-Heredia et al., 2016).

The present water mass analysis was conducted for the JC150 "Zinc, Iron and Phosphorus co-Limitation" GEOTRACES process study (GApr08). This cruise departed Point-à-Pitre, Guadeloupe on June 27, 2017 and arrived at Santa Cruz, Tenerife on August 12, 2017. The transect is located at the southern end of the North Atlantic Subtropical gyre (Fig. 1) on both sides of the Mid-Atlantic Ridge (MAR, ~ 22 °N, ~ 58–31 °W). The JC150 section was specifically studied to understand how a low phosphate environment could lead to zinc-phosphorus and iron-phosphorus co-limitation on nitrogen fixation (Browning et al., 2017; Mahaffey et al., 2014; Moore et al., 2009; Snow et al., 2015; Wu et al., 2000). In this context, the trace metals iron, zinc and aluminum, were measured. The aim of the present water mass analysis is two-fold. Firstly, it aims to provide a detailed understanding of the contribution and distributions of the water masses that exist along the zonal section as well as new constraints in water mass circulation in the subtropical North Atlantic that might be of general interest. Secondly, it aims to provide the tools to efficiently combine this hydrodynamic knowledge with the biogeochemical knowledge from the GEOTRACES program. To achieve this objective, all the OMPA end-members were chosen from GEOTRACES cruises with available zinc, iron, and aluminum concentrations. This enables the estimation of transport and mixing of these elements. Such a choice is a first to the best of our knowledge, and it is now possible thanks to the great extent of the GEOTRACES program.

This study presents the hydrographic properties measured during JC150, including potential temperature, salinity, and the concentration of oxygen and nutrients (θ, S, O_2, NO_3^-, PO_4^{3-}, and

94 $Si(OH)_4$) along with a water mass analysis based on an OMPA and a LPTE.

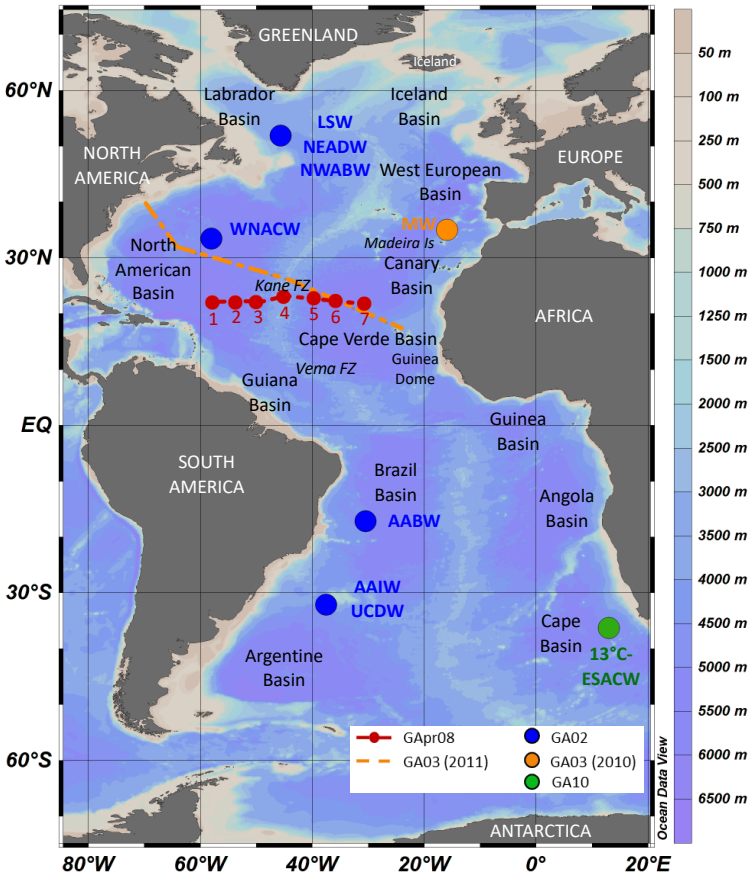

95

96 **Fig. 1.** Map of the JC150 cruise (red dots); locations where the end-members are defined (blue
97 dots - GA02, orange dot - 2010 GA03, and green dot - GA10), and track of the 2011 GA03 cruise
98 (orange dashed line). Refer to Table. 1 for water mass acronyms.

99

100 ## 2 Materials and Methods

101 ### 2.1 Hydrography and nutrients

102 The samples for nutrients, oxygen, and salinity analyses were collected using 24, 10 L trace metal
103 clean Teflon-coated OTE (ocean test equipment) bottles with external springs, mounted on a

titanium rosette and deployed on a Kevlar-coated conducting wire. A SeaBird 911plus CTD recorded the temperature, conductivity, and pressure at 24 Hz with an accuracy of ± 0,001 °C, ± 0,0003 S/m, and ± 0,015 %, respectively. An SBE43 oxygen sensor measured the dissolved oxygen concentration. Standard SeaBird processing routines were used to extract the raw data. The effect of thermal inertia on the conductivity was removed, and a correction was applied for deep oxygen hysteresis (https://www.bodc.ac.uk/resources/inventories/cruise_inventory/reports/jc150.pdf).

After rosette recovery, the OTE bottles were transferred into a class 1000 clean air shipboard laboratory for sampling. The samples for dissolved oxygen and salinity analyses were collected to calibrate the CTD sensors. For the measurements of dissolved oxygen, triplicate samples from 12 depths were fixed immediately and analyzed within 48 h of collection. The samples were analyzed with an automated titrator (Metrohm titrando Titrator). A platinum electrode was used for the potentiometric analysis of Winkler titration. The salinity samples were collected at 6 depths on each cast and analyzed using Guildline's Autosal 8400B. The salinity and oxygen sensors were then calibrated using bottle derived salinity and bottle derived oxygen, which resulted in linear regressions for salinity (calibrated salinity = CTD salinity * 1.0012 - 0.0439) and oxygen (calibrated oxygen (μmol kg^{-1}) = CTD oxygen * 0.9768 + 5.3398). The salinity and oxygen data used in this study were the sensor calibrated data obtained with an accuracy of 0,0001 for salinity and 0,5 μmol kg^{-1} for oxygen. With measurements of calibrated oxygen, salinity, and potential temperature, we calculated the apparent oxygen utilization (AOU) (AOU (μmol kg^{-1}) = saturated oxygen (μmol kg^{-1}) - calibrated oxygen (μmol kg^{-1})). For the AOU calculation, we employed a script, which is originally part of the oceanography toolbox v1.4 compiled by R. Pawlowicz and now available on the MBARI website (https://www.mbari.org/products/research-software/matlab-scripts-oceanographic-calculations/).

127 The samples for nutrient analyses were collected unfiltered into acid-cleaned 60 mL HDPE
128 Nalgene bottles from each OTE bottle. Immediately after collection, they were analyzed through
129 colorimetric procedures (Woodward and Rees, 2001) using clean handling GO-SHIP protocols
130 (Hydes et al., 2010). The micromolar nutrient concentrations were measured using a segmented
131 flow colorimetric auto-analyzer: the PML 5-channel (nitrate, nitrite, phosphate, silicic acid, and
132 ammonium) Bran and Luebbe AAIII system. The instrument was calibrated with nutrient stock
133 standards, and the accuracy was determined using Certified Nutrient Reference Materials (batches
134 CA and BU) obtained from KANSO Technos, Japan. The nano-molar nitrate, nitrite, and
135 phosphate concentrations were analyzed through the segmented flow colorimetric technique that
136 improved the analytical detection limits by using a two-meter liquid waveguide as the analytical
137 flow cell. The same colorimetric method as for the micromolar system was used for analyzing
138 nitrate and nitrite, while the method described in (Zhang & Chi, 2002) was used for analyzing
139 phosphate. The nutrient data presented in this study were measured with an uncertainty of 2%.
140

141 2.2 An extended optimum multiparameter analysis (eOMPA)

142 An eOMPA was used to resolve the water mass structure along the JC150 section (Mackas et al.,
143 1987; Poole & Tomczak, 1999; Tomczak, 1981; Tomczak & Large, 1989). This analysis assumes
144 that the waters sampled along a section result from the mixing of several well-defined water
145 masses, called the source water types or end-members. The degree of mixing and the contribution
146 of each end-member is solved using an optimization procedure. Mathematically, an OMPA is an
147 optimal solution to a linear system of mixing equations with the contribution of end-members as
148 variables and the conservative hydrographic properties as the parameters of the system. This model
149 optimizes, for each data point (sample), the end-member parameter contributions to reproduce the

observational data. The OMPA is performed as an overdetermined system using non-negative least square optimization.

In OMPA, the hydrographic properties are used as parameters in the equation system. In this study, the available parameters are as follows: potential temperature (θ), salinity (S), concentration of dissolved oxygen (O_2), phosphate (PO_4^{3-}), nitrate (NO_3^-), and silicic acid ($Si(OH)_4$), and mass conservation (the sum of all contributions must be equal to unity). A classical OMPA resolves the system assuming that all those parameters are conservative, i.e., they have no sources or sinks in the ocean interior. This assumption was not acceptable for O_2, NO_3^-, and PO_4^{3-} in our case, as the end-members were defined at the Atlantic basin-wide scale and thus highly susceptible to organic matter remineralization. To consider these biogeochemical processes, we realized an eOMPA for this study. Most eOMPA studies use the quasi-conservative N* and P* parameters (García-Ibáñez et al., 2018; Jenkins et al., 2015). We preferred to adopt the parameters PO and NO defined in Broecker (1974) using the following equations, because unlike P* and N*, PO and NO do not require any assumption about initial gas equilibrium at the air/sea interface. Other recent studies have also made this choice (Álvarez et al., 2014; Peters et al., 2018).

$$PO = [O_2] + R_{O2/P} * [\ PO_4^{3-}], \quad (1)$$

$$NO = [O_2] + R_{O2/N} * [\ NO_3^-], \quad (2)$$

where $R_{O2/P}$ and $R_{O2/N}$ are Redfield ratios that estimate the number of O_2 moles consumed for one mole of PO_4^{3-} and NO_3^- released during the process of organic matter remineralization, respectively (Anderson & Sarmiento, 1994). In this manner, and under the assumption that the Redfield ratios $R_{O2/P}$ and $R_{O2/N}$ are accurate, remineralization has no impact on PO and NO. However, it is important to note that the Redfield ratios are spatiotemporally variable and have

been revised since their original definition. Therefore, we qualified PO and NO as quasi-conservative. In this study, we defined $R_{O2/P}$ = 155 and $R_{O2/N}$ = 9.69, in the range of Anderson (1995), and similar to the values used by Peters et al. (2018).

These definitions combine the three non-conservative parameters O_2, PO_4^{3-}, and NO_3^- into two quasi-conservative parameters PO and NO. Transforming three parameters into two reduces the rank of the mixing equation system by one and thereby the number of end-members that can be considered.

The conservative character of the $Si(OH)_4$ parameter is also questionable. At depth, the biogenic particulate matter degradation releases $Si(OH)_4$. Unlike PO_4^{3-} and NO_3^-, the $Si(OH)_4$ parameter cannot be corrected using the Redfield ratio, as it is not linked to organic matter remineralization, but to biogenic opal dissolution. In the Atlantic, the magnitude of the $Si(OH)_4$ excess from opal dissolution has been estimated to represent only 5% of the difference between the $Si(OH)_4$ concentrations of the northern and southern end-members. Therefore, the opal dissolution effect on water mass properties is insignificant compared to the effect of water mass mixing at the basin scale (Broecker et al., 1991). Thus, the $Si(OH)_4$ concentration was considered as a conservative parameter in this study.

The parameters considered to resolve the eOMPA in this work were as follows: θ, S, PO, NO, $Si(OH)_4$, and mass conservation. This led to the following system of mixing equations applied at each sample point with (n) end-members:

$$X_1\theta_1 + X_2\theta_2 + \ldots\ldots + X_n\theta_n = \theta_{sample} + \varepsilon_\theta, \quad (3)$$

$$X_1S_1 + X_2S_2 + \ldots\ldots + X_nS_n = S_{sample} + \varepsilon_{S,} \quad (4)$$

$$X_1PO_1 + X_2PO_2 + \ldots\ldots + X_nPO_n = PO_{sample} + \varepsilon_{PO}, \quad (5)$$

$$X_1NO_1 + X_2NO_2 + \ldots\ldots + X_nNO_n = NO_{sample} + \varepsilon_{NO}, \quad (6)$$

$$X_1\ Si(OH)_{4,1} + X_2\ Si(OH)_{4,2} + \ldots\ldots + X_n\ Si(OH)_{4,n} = Si(OH)_{4,sample} + \varepsilon_{Si(OH)4}, \quad (7)$$

$$X_1 + X_2 + \ldots\ldots + X_n = 1 + \varepsilon_x, \quad (8)$$

$$Xi \geq 0, \quad (9)$$

where the variables X_1–X_n (n = each end-member) denote the contribution of the end-members, and ε_θ, ε_S, ε_{PO}, ε_{NO}, $\varepsilon_{Si(OH)4}$, and ε_x are the residuals, i.e., the difference between the calculated and observed values. The eOMPA was performed using the OMPA V2.0 MATLAB package developed by Johannes Karstensen and Matthias Tomczak (https://omp.geomar.de).

As the OMPA should be performed as an overdetermined system, the number of end-members must be strictly lower than that of available parameters. A total of six parameters were considered in this study; however, over five end-members probably contributed to the water masses found along the JC150 section. To solve this problem, we first tried to increase the number of parameters used. However, no other conservative (or quasi-conservative) tracer was available in the JC150 cruise. We considered adding the potential vorticity as a quasi-conservative tracer. However, the profiles were observed to be excessively noisy, and despite many filtration attempts, we could not deduce an approach to obtain benefits from the use of this parameter in the eOMPA calculation. Therefore, we did not include this parameter. Another way to include over five end-members is to divide the water column into several layers, because some end-members impact only certain depth layers. The zonal section was therefore divided into three density layers with the following isopycnals: 26.50 kg m^{-3}–27.30 kg m^{-3} (thermocline layer), 27.30 kg m^{-3}–27.75 kg m^{-3} (intermediate layer) and > 27.75 kg m^{-3} (deep layer). These density layers broadly corresponded

to depths of 300–700 m (thermocline layer), 700–1500 m (intermediate layer), and 1500 m to seafloor (deep layer). An eOMPA was then applied independently to each of these layers. Waters above ~300 m were excluded from the eOMPA for two reasons: firstly, the hydrographic parameters, including θ and S were non-conservative in the mixed layer (mean annual maximum ~120 m at 22°N, http://mixedlayer.ucsd.edu, Holte et al., 2017); secondly, these waters were warmer and saltier than any well-defined end-member in the literature (Fig. 2). To precisely define the boundaries between the density layers (thermocline, intermediate, and deep layers), the samples located close to the layer boundaries were executed in both the overlying and underlying eOMPAs (both thermocline and intermediate eOMPAs and both intermediate and deep eOMPAs). The boundaries of the density layers were chosen where the smallest residuals were obtained. This procedure was performed, similar to those reported by Kim et al. (2013) and Peters et al. (2018). With the availability of six parameters, five end-members can be considered in each layer. We carefully selected them through an in-depth literature review, comparison of the JC150 hydrographic section properties with those of the end-member candidates, and interpretation of the LPTE results (see section 3.2). In this study, the end-member characteristics were all selected from GEOTRACES cruises in the core of the water masses and with intervals of variations established by comparison with nearby data areas (refer to Table. 1). These intervals are specific to each of the properties of each end-members and reflect the natural variability of end-member characteristics (temporal, spatial). Perturbation analyses are presented below.

The eOMPA parameters were weighted according to their signal to noise ratios (measurement accuracy compared to the range of variation among end-members) and conservative character (conservative or quasi-conservative). In most studies, this led to assigning higher weights to θ, S,

and mass conservation than NO_3^-, PO_4^{3-} (or NO, PO), and $Si(OH)_4$. The mass conservation usually receives the same weighting as the parameter with the highest weight (Poole & Tomczak, 1999; Tomczak & Large, 1989).

In this work, different weightings were tested, starting from a uniform value for all parameters to 16 times higher weighting for θ, S, and mass conservation than PO, NO, and $Si(OH)_4$. The minimum residuals were obtained for the following weightings: 24 for θ, 24 for S, 2 for PO, 2 for NO, 2 for $Si(OH)_4$, and 24 for mass conservation. To compare the residuals of different parameters (for instance, θ and S), we expressed these residuals as percentages of the parameter ranges over the entire layer (Fig. S4).

To validate the reliability and robustness of the eOMPA results obtained in this study, a series of perturbation tests (Monte Carlo analysis) were realized. These tests allowed to estimate the extent to which the eOMPA results could be affected by the variability of 1) the end-member characteristics, 2) JC150 data (including the Redfield ratio used to calculate NO and PO), and 3) the chosen weights. For each test, 100 runs were performed in each eOMPA layer. For each run, perturbations were applied to targeted parameters (end-members, JC150 data, or weights) using normal probability density functions with standard deviations scaled to the uncertainty (or variability) attributed to each parameter. For the first test, uncertainties were the end-member property definition intervals, which reflected the possible variation in the end-member characteristics (reported in Table. 1). For the second test, the JC150 data uncertainties were used, i.e., the sensor uncertainties (0,001 for θ, 0,0001 for S, and 0,5 μmol Kg^{-1} for O_2) and the nutrient measurement uncertainties (2% for PO_4^{3-}, NO_3^-, and $Si(OH)_4$). For this test, the Redfield ratios used to define NO and PO were also modified within a 10% range (155 +/- 15 for $R_{O2/P}$, 9,69 +/-

1 for $R_{O2/N}$), which was consistent with reported Redfield ratio variability (Anderson, 1995; Anderson & Sarmiento, 1994). For the third test, the weights were modified within the range of 24 +/- 5 for θ and S and 2 +/- 0,7 for PO, NO, and $Si(OH)_4$. 1000 perturbations were also performed for the first two tests, and the results obtained (not shown here) were very similar to those obtained with 100 perturbations.

Acronym	Name	Θ (°C)	S	O2 (µmol Kg^{-1})	[PO_4^{3-}] (µmol Kg^{-1})	[NO_3^-] (µmol Kg^{-1})	Si (µmol Kg^{-1})	'PO' (µmol Kg^{-1})	'NO' (µmol Kg^{-1})	Data sources	eOMPA layer
WNACW	West North Atlantic Central Water	17.94 ± 0.1	36.545 ± 0.02	202.30 ± 11	0.13 ± 0.04	3.10 ± 1.2	1.40 ± 0.6	222 ± 16	232 ± 16	GA02 station 18, 22/05/2010, 33.433°N, 58.05°W, 251m	T
ESACW	East South Atlantic Central Water	12.20 ± 0.2	35.117 ± 0.15	205.20 ± 1	0.80 ± 0.04	11.89 ± 2	5.01 ± 1	330 ± 3	320 ± 28	GA10 station 3, 29/12/2011, 36.348°S, 13.140°E, 497m	T&I
MW	Mediterranean Water	10.13 ± 0.4	35.920 ± 0.1	178.10 ± 8	1.06 ± 0.01	16.67 ± 0.2	10.43 ± 0.5	342 ± 3	340 ± 3	GA03 station 3, 19/10/2010, 35.201°N, 16°W, 986m	T&I&D
AAIW	Antartic Intermediate Water	3.89 ± 0.3	34.290 ± 0.05	218.30 ± 10	2.05 ± 0.12	30.29 ± 1.5	28.08 ± 8	536 ± 8	512 ± 6	GA02 station 9, 14/03/2011, 32.089°S, 37.459°W, 1001m	T&I
UCDW	Upper Circumpolar Deep Water	2.84 ± 0.03	34.576 ± 0.08	186.90 ± 5	2.18 ± 0.05	31.93 ± 0.7	54.78 ± 1.7	525 ± 16	496 ± 10	GA02 station 9, 14/03/2011, 32.089°S, 37.459°W, 1501m	T&I
LSW	Labrador Sea Water	3.76 ± 0.15	34.896 ± 0.04	272.30 ± 6	1.09 ± 0.05	16.70 ± 0.3	9.40 ± 0.8	441 ± 3	434 ± 64	GA02 station 9, 09/05/2010, 51.821°N, 45.732°W, 996m	I&D
NEADW	North East Atlantic Deep Water	2.66 ± 0.09	34.917 ± 0.003	273.20 ± 5	1.08 ± 0.02	16.40 ± 0.2	14.00 ± 1.9	441 ± 2	432 ± 3	GA02 station 9, 09/05/2010, 51.821°N, 45.732°W, 2512m	D
NWABW	North West Atlantic Bottom Water	1.63 ± 0.02	34.896 ± 0.09	290.50 ± 0.2	0.98 ± 0.01	14.70 ± 0.1	11.20 ± 0.1	442 ± 0.6	433 ± 0.8	GA02 station 9, 09/05/2010, 51.821°N, 45.732°W, 4041m	D
AABW	Antartic Bottom Water	0.04 ± 0.06	34.680 ± 0.01	217.40 ± 1.9	2.26 ± 0.07	32.72 ± 0.7	122.80 ± 4.5	568 ± 9	534 ± 4	GA02 station 13, 20/03/2011, 17.017°S, 30.599°W, 4889m	D

Table. 1. End-member definitions (values ± uncertainties) from GEOTRACES cruises (refer to the GA03 special issue, Boyle et al., 2015; GA02 papers, Middag et al., 2015; and Rijkenberg et al., 2014). Each end-member is included into one or more of the three extended optimum multiparameter analysis (eOMPA) layers - T: Thermocline, I: Intermediate, and D: Deep. To facilitate the future use of this eOMPA for biogeochemical studies, trace elements and some isotope data are available for each end-member on the GEOTRACES Intermediate Data Product 2017 (IDP 2017 v2, Schlitzer et al., 2018).

2.3 LPTE

To improve the proposed water mass analysis, LPTEs were conducted to complement the eOMPA (i) to aid in identifying the origin of the water masses sampled along JC150 (and thereby contribute

to the eOMPA end-member choices) and (ii) to provide information about water mass trajectories between their formation areas and the JC150 section, which cannot be achieved by a sole OMPA. The LPTE experiments were conducted in the velocity field of an eddy-resolving Ocean General Circulation Model. Through the seeding of numerous 'virtual' particles around a point and time of interest (i.e., latitude, longitude, depth, and time), the LPTE can track the particles' location through reverse time by updating the particles' position after each time step of the model. This method enables us to identify the particles' origin over timescales from tens to hundreds of years and reconstruct the trajectories of these particles from the position of origin to the point of interest. As the particles deployed are all marginally offset in space and time relative to the exact sampling position, they generate an ensemble of backward trajectories and origins that can assist in identifying likely water masses constituting the sampled seawater. The model and experiments used in this study are described below.

The velocity fields of the Operational Mercator global ocean analysis and forecast system (http://marine.copernicus.eu) were used in this study. This system uses the Ocean General Circulation Model from the Nucleus for European Modelling of the Ocean (NEMO) framework (Madec & the NEMO team, 2008) with a horizontal resolution of 1/12° and 50 vertical layers. The thickness of each vertical layer increases with depth from 1 m at the surface to 450 m at the bottom (5500 m depth). Partial steps were used for the bottom grid cell of the water column to better represent the bottom topography within the model. The model topography was generated with the bathymetric databases ETOPO2 (Amante & Eakins, 2009) and GEBCO8 (Becker et al., 2009) for open ocean and continental shelves, respectively. For further details on the model product and the validity of its velocity fields, the reader can refer to Lellouche et al. (2018a) and Lellouche et al.

(2018b). The velocity fields are available as daily and monthly mean values from 26 December 2006 to present.

The Lagrangian experiments were conducted for each sample obtained from the seven stations (total of 302 samples) occupied during the 40-day JC150 cruise (Fig. 1) using the Lagrangian particle tracking tool ARIANE (Blanke & Raynaud, 1997).

As currents are faster in the upper ocean (defined here as the top 800 m), and capturing their behavior requires a finer time resolution, different experimental configurations were defined for each sample based on its sampling depth. Firstly, for depths shallower than 800 m, we employed daily mean velocity fields to track the deployed particles, whereas for depths deeper than 800 m, we used monthly mean values. Secondly, the particles were advected backward in time for varied periods depending on the depth: up to 10 years for the upper ocean samples and up to 300 years for the deep ocean ones.

In all cases, an ensemble of particles (or particle clouds) was uniformly distributed around the sampling location and repeatedly deployed across a period that was centered on the sampling time. This ensemble was organized as a vertical cylinder, made of equally spaced disks of particles spaced at 1/12° resolution radially.

The height of the cylinder, number of disks inside each cylinder, and the number of repeated releases around the sampling time varied between the samples taken within the upper or deep ocean. For example, for the upper ocean, we used a cylinder with a height of 10 m and radius of ¼° and 12-hourly release of particles within a five-day window (nine releases). More details about

this experimental setup are provided in S1, while several examples of particle trajectory ensembles for different depths and advection times are shown in Figure S2.

3 Water mass analysis: results and discussion

The hydrographic properties measured during JC150, θ, S, AOU, and concentrations of O_2, PO_4^{3-}, NO_3^-, and $Si(OH)_4$, are presented in this study for the first time. They are shown as property/property plots in Figure 2, and as section in Figure 3.

The discussion is organized in three parts. Firstly, the surface waters shallower than 200–300 m (where an eOMPA cannot be performed, because water properties are constantly changing due to ocean-atmosphere exchange) are discussed using satellite data and LPTE results. Secondly, the end-member choice for the three eOMPA layers is extensively discussed using a thorough literature review, meticulous comparison of the JC150 hydrographic section properties with those of the end-member candidates, and the LPTE results. Finally, the results of the eOMPA are presented (end-members contributions) and discussed.

The LPTE results are presented in Figure 4. It is beyond the scope of this study to present the LPTE results across all stations and depths. Therefore, for discussion, we selected results at specific depths and from stations 1 and 7, representing the westernmost and easternmost stations, respectively. Finally, the results from the eOMPA are presented in Figure 5.

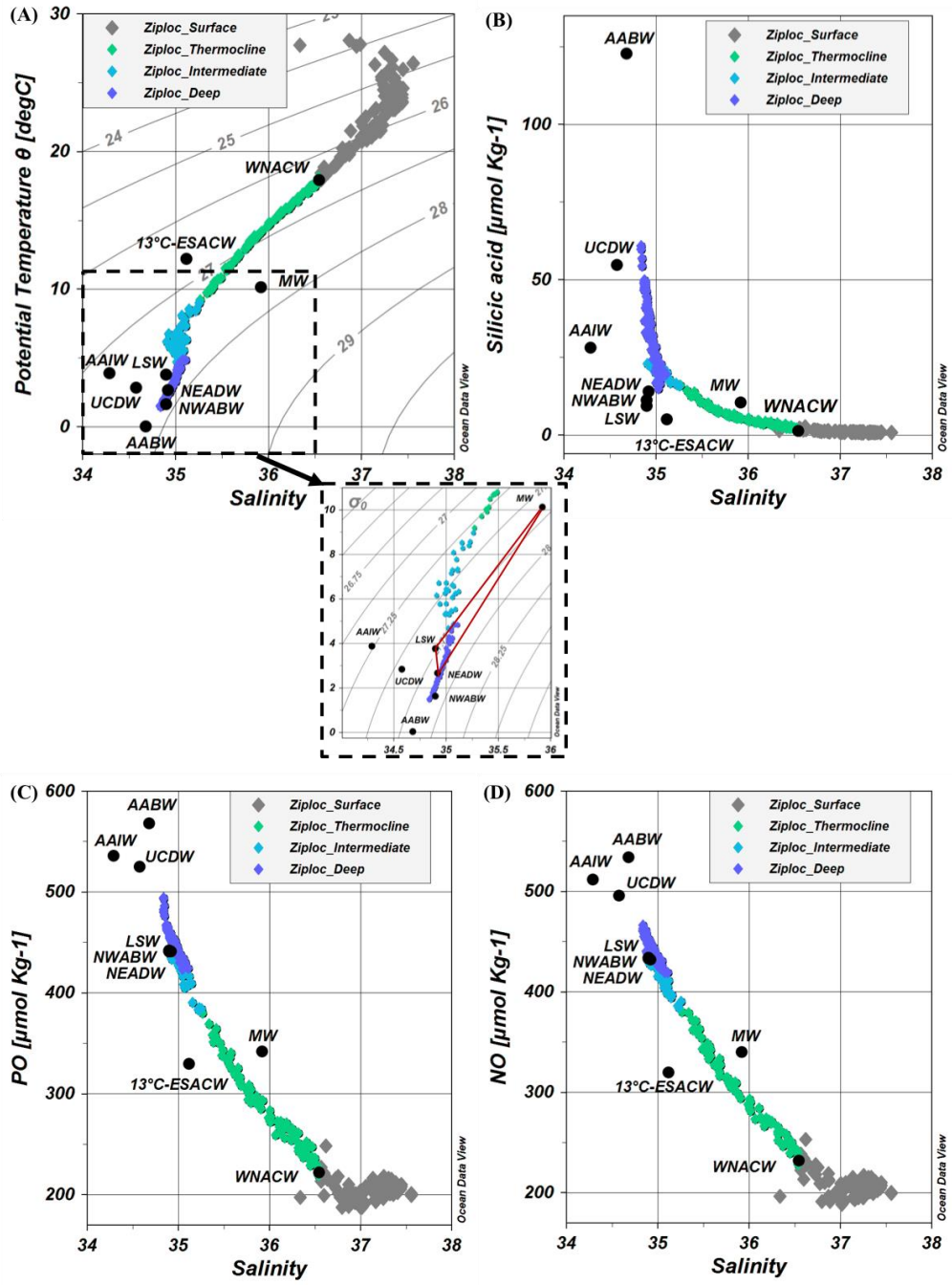

Fig. 2. Potential temperature versus salinity with isopycnals (gray lines) and a zoom on water colder than 10 °C, in which the red triangle highlights the impact of Mediterranean Water (MW) in the deep layer (A), silicic acid versus salinity (B), PO versus salinity (C), and NO versus salinity (D) for the JC150 data (color diamonds) and GEOTRACES end-members (black diamonds). PO and NO definitions are provided in section 2.2.

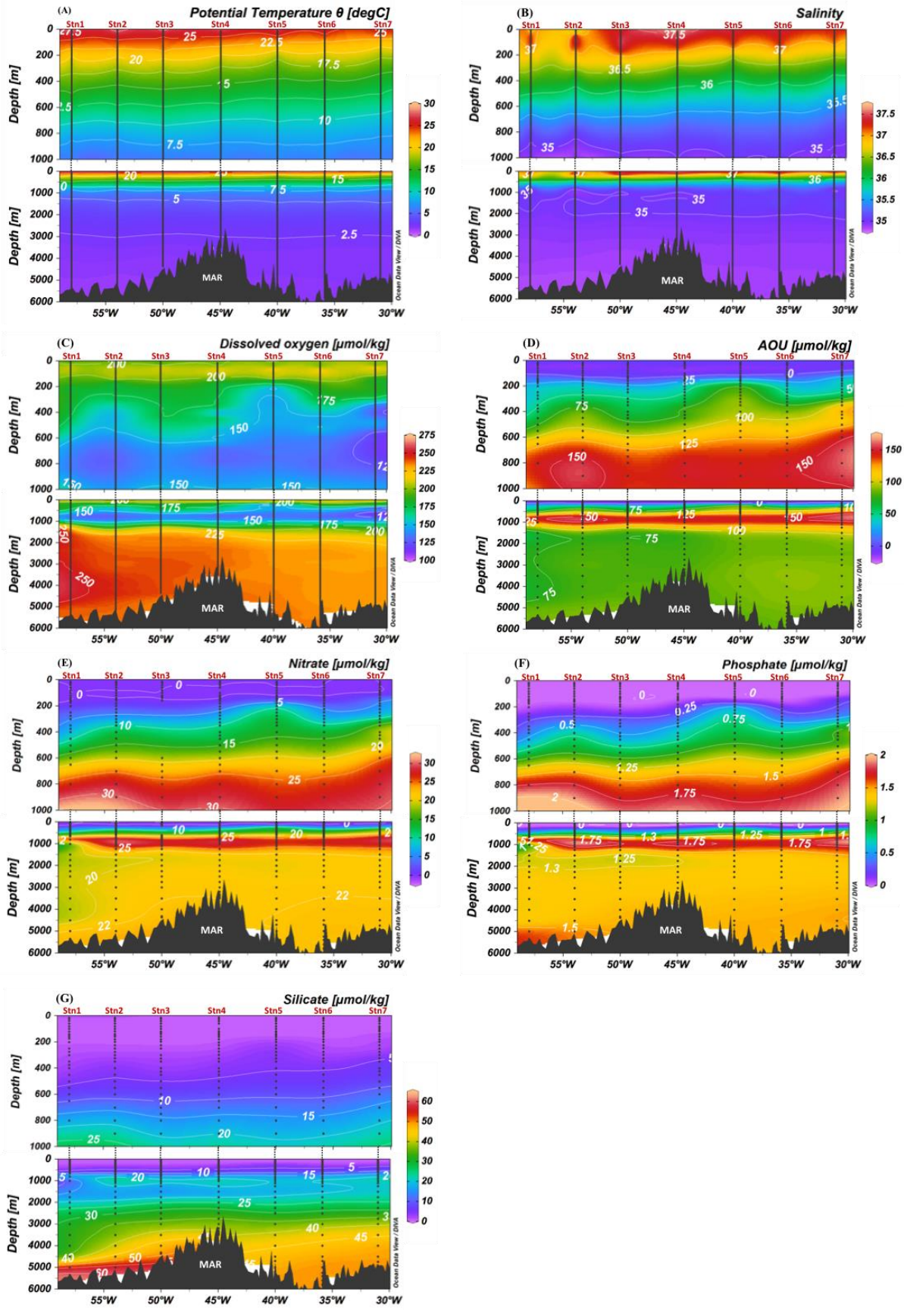
(A)
Potential Temperature θ [degC]
(B)
Salinity
(C)
Dissolved oxygen [µmol/kg]
(D)
AOU [µmol/kg]
(E)
Nitrate [µmol/kg]
(F)
Phosphate [µmol/kg]
(G)
Silicate [µmol/kg]
Stn1
Stn2
Stn3
Stn4
Stn5
Stn6
Stn7
Depth [m]
MAR
55°W
50°W
45°W
40°W
35°W
30°W
Ocean Data View / DIVA

345

Fig. 3. Observed section of potential temperature (A), salinity (B), dissolved oxygen (C), apparent oxygen utilization (AOU, D), and concentrations of nitrate (E), phosphate (F), and silicic acid (G) from the JC150 cruise. The upper figures show zooms on the upper 1000 m, while the lower figures show the full depth range. Data points are represented by black dots.

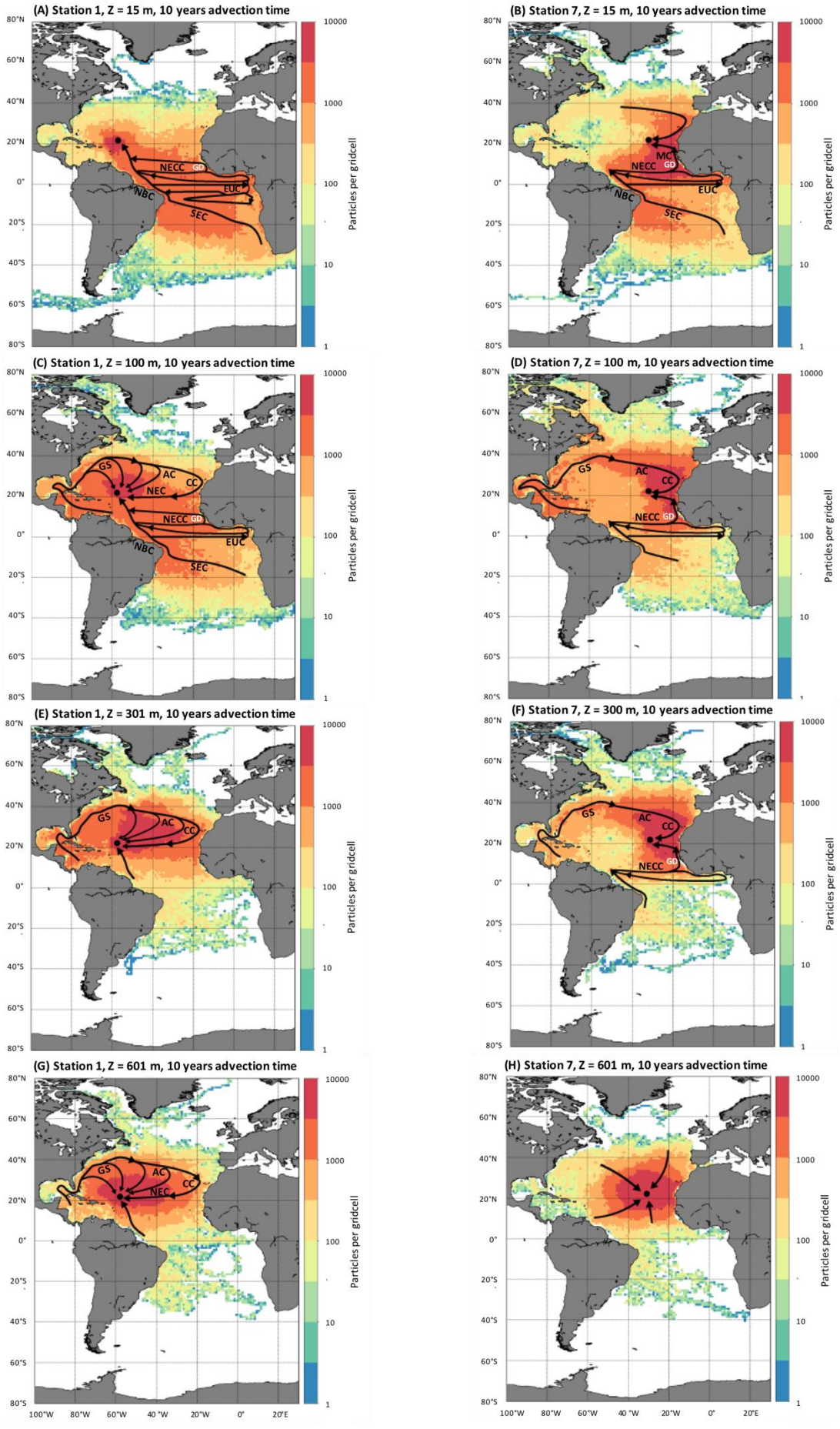
(A) Station 1, Z = 15 m, 10 years advection time
(B) Station 7, Z = 15 m, 10 years advection time
(C) Station 1, Z = 100 m, 10 years advection time
(D) Station 7, Z = 100 m, 10 years advection time
(E) Station 1, Z = 301 m, 10 years advection time
(F) Station 7, Z = 300 m, 10 years advection time
(G) Station 1, Z = 601 m, 10 years advection time
(H) Station 7, Z = 601 m, 10 years advection time
NECC
GD
NBC
EUC
SEC
MC
GS
AC
CC
NEC
Particles per gridcell
10000
1000
100
10
1
80°N
60°N
40°N
20°N
0°
20°S
40°S
60°S
80°S
100°W
80°W
60°W
40 °W
20°W
0°
20°E

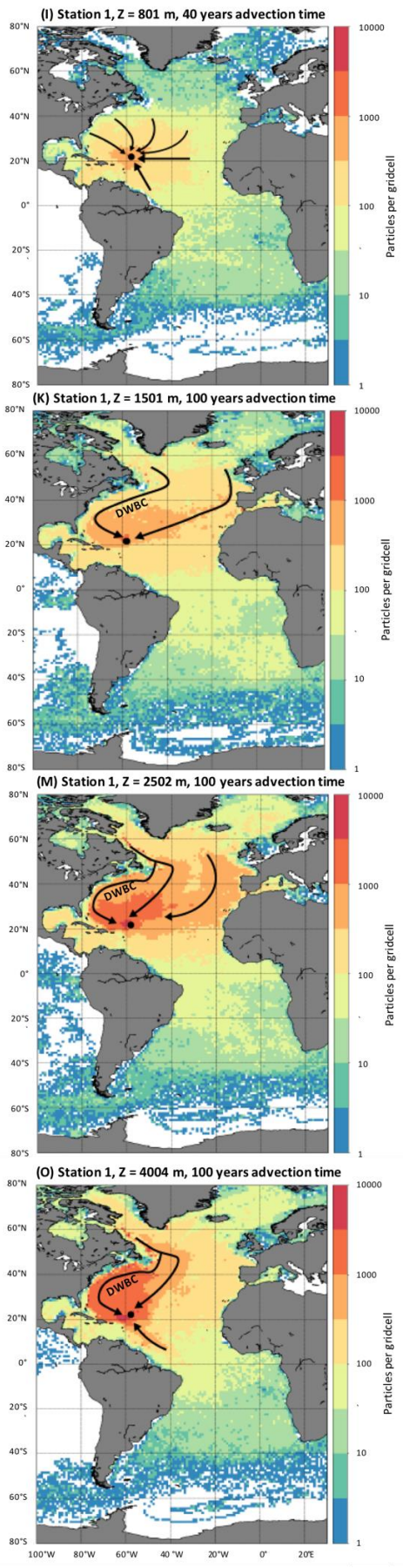
(I) Station 1, Z = 801 m, 40 years advection time
(J) Station 7, Z = 801 m, 40 years advection time
(K) Station 1, Z = 1501 m, 100 years advection time
(L) Station 7, Z = 1501 m, 100 years advection time
(M) Station 1, Z = 2502 m, 100 years advection time
(N) Station 7, Z = 2502 m, 100 years advection time
(O) Station 1, Z = 4004 m, 100 years advection time
(P) Station 7, Z = 4004 m, 100 years advection time
DWBC
Particles per gridcell
10000
1000
100
10
1
80°N
60°N
40°N
20°N
0°
20°S
40°S
60°S
80°S
100°W
80°W
60°W
40 °W
20°W
0°
20°E

Fig. 4. Particle counts per 2° x 2° grid cells computed by the Lagrangian particle tracking experiment (LPTE), indicating particle origins and particles' most-used pathways to attain the sampling locations. Results are presented for two JC150 stations (westernmost station 1, 22 °N, 58 °W, left panels and easternmost station 7, 22 °N, 31 °W, right panels) and different depths. Particles are advected backward in time with an advection time varying with depth. Arrows highlight the main particle paths obtained from the LPTE results and literature general knowledge. The following currents and location are presented in the figures: Gulf Stream (GS), Azores Current (AC), Canary Current (CC), North Equatorial Current (NEC), South Equatorial Current (SEC), North Brazil Current (NBC), Equatorial Undercurrent (EUC), North Equatorial Countercurrent (NECC), Mauritania Current (MC), Deep Western Boundary Current (DWBC) and Guinea Dome (GD). Refer to Fig. S2 for corresponding raw trajectories.

3.1 Surface waters

At the western edge of the section, a near surface tongue of low salinity water (36.3–37) is observed shallower than 27 m at stations 1 and 2 (Fig. 3b). Using a surface satellite salinity map (SMOS, July 2017, Fig. S3), this feature can clearly be attributed to Amazon River plume. This is supported by the LPTE results that show the particle trajectories from near the Amazon River mouth reaching the west of the zonal section (at depths of 15 m and 100 m, as shown in Figs. 4a and 4c, respectively). This feature is constrained to the very surface and does not impact the eOMPA results discussed below.

Two well-defined central water masses dominate the tropical Atlantic thermocline layer: the North Atlantic Central Water (NACW) and the South Atlantic Central Water (SACW). The sampled

section extends along 22 °N, 58–31 °W, while the transition from NACW into SACW occurs at approximately 15 °N at the Cape Verde Frontal Zone (Fieux, 2010; Tomczak & Godfrey, 1994). Therefore, the impact of NACW and SACW on the sampled waters was investigated.

SACW encompasses two main water masses, including the Western SACW (WSACW) and the Eastern SACW (ESACW) (Poole & Tomczak, 1999). WSACW is formed in the confluence zone of Brazil and Malvinas Currents (Fieux, 2010) and recirculates within the southern subtropical gyre. Therefore, it is mostly restricted to the western South Atlantic Ocean (Fieux, 2010; Tomczak & Godfrey, 1994). In contrast, ESACW mainly comprises Indian Central Water transferred into the Atlantic Ocean through Agulhas Current rings and is known to cross the Atlantic basin several times during its northwards transit (Fieux, 2010; Tomczak & Godfrey, 1994; Tsuchiya, 1986). Our LPTE trajectories are in good agreement with the current understanding of the ESACW northward transit (Figs. 4a–4d): ESACW is transported northwestwards from the Cape Basin to the equator through the southern branch of the South Equatorial Current and North Brazil Current. Here, the trajectories show a portion of ESACW continuing northward toward the western stations (Figs. 4a and 4c), while a portion retroflects eastward toward the Guinea Dome within components of the equatorial current system (Figs. 4a–4d).

In addition to what has been previously described, the LPTE suggested that this shallow ESACW reached the JC150 zonal section from the Guinea Dome by two trajectories: a portion flows northwards within the Mauritania Current to the easternmost stations (Figs. 4b and 4d), while another portion crosses the Atlantic basin westward once more and then flows northward to join the westernmost stations (Figs. 4a and 4c).

NACW also comprises several waters masses. More than half of its volume comprises subtropical mode water (Tomczak & Godfrey, 1994). The principal North Atlantic's subtropical mode water is the Western NACW (WNACW, Talley et al., 2011), also called '18 °C water'. WNACW is formed in the Sargasso Sea and identified by a permanent thermostat between 300 and 500 m at approximately 17–18 °C (Fieux, 2010; Tomczak & Godfrey, 1994).

Between 100 and 300 m, the LPTE analysis shows waters following the North Atlantic anticyclonic subtropical gyre circulation, i.e., waters originate from the Gulf of Mexico and the Caribbean Sea, flow through the Sargasso Sea and the Gulf Stream and then the Azores and Canary currents, and finally the North Equatorial Current flowing westward redistributes these waters from the eastern to the western JC150 stations. In addition, the LPTE trajectories show a direct transfer from the Gulf Stream to the sampled stations (Figs. 4c–4f). These trajectories correspond very well to the circulation pattern of WNACW. This suggests that this 100 to 300 m depth layer, below the layer mainly occupied by ESACW, is dominated by WNACW.

In summary, above ~300 m, the salinity data from JC150, SMOS, and LPTE show an Amazon influence in the west of the section, which is restricted to the near-surface. The LPTE results highlight the dominant influence of a shallow variety of ESACW in the upper 100 m and an increasing WNACW impact below 100 m.

3.2 Analysis of end-members for thermocline, intermediate, and deep eOMPA layers

This section discusses the end-member choice for the thermocline (main thermocline from 300–700 m), intermediate (700–1500 m) and deep eOMPA layers (1500 m to seafloor).

All end-members of the present eOMPA were selected from GEOTRACES cruises, where numerous parameters, including trace elements and isotopes, are available to facilitate further use of this eOMPA results (these locations are not necessarily in the water mass formation regions).

3.2.1 Thermocline waters

The two central waters discussed above (ESACW and WNACW) are also present below 300 m. WNACW is the only water mass that can account for the warm, salty, and low PO and NO concentration waters found in the thermocline layer (Fig. 2). In addition to supporting the presence of WNACW in surface waters (section 3.1), the LPTE analysis supports the large contribution of WNACW to the thermocline layer (Figs. 4e–4h) with particles following the anticyclonic North Atlantic Subtropical gyre circulation between 300–600 m (refer to WNACW circulation details in section 3.1). Although the surface gyre circulation pattern appears weaker by 800 m (Figs. 4i and 4j), WNACW is ultimately an important end-member to be included in the thermocline layer. We used θ, S, concentrations of O_2, PO_4^{3-}, NO_3^-, and $Si(OH)_4$ data from the GEOTRACES GA02 cruise station 18 at ~250 m to define WNACW (Fig. 1). These end-member hydrographic and nutrient values are in agreement with those reported in literature (Hinrichsen & Tomczak, 1993; Talley et al., 2011, cf. Table.1 for detailed properties). As stated earlier (section 3.1), WNACW is the main type of NACW. Other types of NACW, such as the Madeira Mode Water or the East NACW, exist (Harvey, 1982; Talley et al., 2011; Tomczak & Godfrey, 1994). However, the Madeira Mode Water presents a formation rate and volume, which are much lower than those of WNACW. The East NACW is considered in this study as partly included in the Mediterranean Water (MW) definition (refer below, Carracedo et al., 2016; Talley et al., 2011). Therefore,

Madeira Mode Water and East NACW were not included as an end-member in the present eOMPA.

A type of ESACW, namely the 13 °C-ESACW, is an important contributor to the thermocline of the Atlantic Ocean (Tomczak & Godfrey, 1994; Tsuchiya, 1986). 13 °C-ESACW is needed to account for the warm, low salinity, and low PO, NO, and $Si(OH)_4$ waters in the thermocline layer, as well as the warm, low salinity, and low PO and NO waters in the intermediate layer (Fig. 2). Even though the LPTE results do not show a dominance of ESACW trajectories below 300 m along the JC150 zonal section (WNACW dominates at 300–800 m), they still show a non-negligible influence from south Atlantic origin waters to depths of 800 m (Figs. 4i and 4j) and 1000 m (data not shown). Therefore, 13 °C-ESACW was chosen as an end-member to be considered in both thermocline and intermediate layers. We used θ, S, concentrations of O_2, PO_4^{3-}, NO_3^-, and $Si(OH)_4$ data from the GEOTRACES GA10 cruise station 3 at ~500 m to define 13 °C-ESACW (Fig. 1). These end-member hydrographic and nutrient values are in agreement with those reported in literature (Poole & Tomczak, 1999, refer to Table. 1 for detailed properties).

As stated earlier (section 3.1), the other major SACW, which is WSACW, is restricted to the southwest Atlantic (south of 30 °S, Fieux, 2010; Tomczak & Godfrey, 1994). This restriction was underlined by a previous OMPA study, in which almost no contribution of WSACW was observed at 22 °N (Poole & Tomczak, 1999). The LPTE results support these conclusions, as they show no significant particles originating from the West South Atlantic, south of 30 °S, at the thermocline depths (Figs. 4e–4h). Therefore, WSACW was not included in the thermocline eOMPA. Note that the Guinea Dome Water was not explicitly included as an end-member in the present eOMPA; however, it was implicitly included, as it could be considered as ESACW significantly modified by the remineralization processes (Stramma & Schott, 1999).

3.2.2 Intermediate waters

At intermediate depths (~700–1500 m), the hydrographic atlases clearly show a high salinity layer, which is attributed to the MW (World Ocean Atlas 2018, Fieux, 2010). MW is formed by the mixing of the Mediterranean Outflow water, entering the Atlantic through the Gibraltar Strait, with the subsurface and intermediate waters of the northeast Atlantic (Baringer, 1997; Carracedo et al., 2016). MW extends northward to the Iceland-Scotland Ridge and westward to the Gulf Stream (core at ~1000 m, Fieux, 2010), thereby presenting an important contribution to intermediate depths across the North Atlantic. However, high salinity MW is not visible along the JC150 section (Fig. 3b). This is because, at ~20 °N, the MW salinity maximum is located at the same depth as low salinity Antarctic Intermediate Water (AAIW), where mixing reduces the salinity (Fieux, 2010; Talley et al., 2011). AAIW is the densest and less salty of the subantarctic mode water. Formed along the subantarctic and mostly in the southeast Pacific, AAIW enters into the Atlantic Ocean mainly via the Drake Passage and the Malvinas Current (Pacific type of AAIW) and expands northward (Fieux, 2010 and references therein; Talley, 1996; Tomczak & Godfrey, 1994). This northward expansion of low salinity AAIW is traced as far as 20 °N between 800–1000 m (Fieux, 2010; Hinrichsen & Tomczak, 1993; Talley et al., 2011). This observation possibly explains the lower salinity (< 35) centered at ~1000 m, mainly observed in the west of the MAR during the JC150 cruise (Fig. 3b). Nevertheless, the θ-S diagram (Fig. 2a) shows that MW is the only intermediate water mass that can explain the cold and saline waters in the thermocline layer and the saltiest waters in both intermediate and deep layers (as previously suggested by Reid, 1979).

Furthermore, a strong O_2 minimum (O_2 < 150 μmol kg^{-1}), which is coincident with a layer of high AOU (AOU > 125 μmol kg^{-1}), is visible across the entire JC150 zonal section centered at ~800 m (Figs. 3c and 3d). This O_2 minimum is also nearly coincident with a layer of maximum NO_3^- and PO_4^{3-} concentrations centered at ~900 m (> 25 μmol kg^{-1} and > 1.5 μmol kg^{-1}, respectively, Figs. 3e and 3f, respectively) and relatively high $Si(OH)_4$ concentration (> 20 μmol kg^{-1}, ~1000 m, Fig. 3g). All these properties reflect the remineralization processes known to characterize the Upper Circumpolar Deep Water (UCDW) originating from the Southern Ocean and flowing northward into the Atlantic just below AAIW (Broecker et al., 1985). In the tropics, AAIW joins vertically with UCDW (Talley et al., 2011; Tsuchiya et al., 1994). The resulting AAIW/UCDW complex, traceable by high nutrients rather than low salinity, moves northward into the Gulf Stream system and North Atlantic Current as far as 60 °N just south of Iceland (Talley et al., 2011; Tsuchiya, 1989; Tsuchiya et al., 1994). This is consistent with the low O_2, high NO_3^-, PO_4^{3-}, and $Si(OH)_4$ layers described above along the JC150 section. In addition, inclusion of AAIW and UCDW are necessary to explain the coldest and highest PO and NO values in both thermocline and intermediate layers (Fig. 2). UCDW is also specifically needed to explain the highest $Si(OH)_4$ values of the intermediate layer.

Although, the LPTE results did not aid us in clearly confirming (nor reject) the contributions of MW, AAIW, and UCDW along the JC150 section, the above discussion is sufficient to conclude that MW was an essential end-member to include in the three eOMPA layers, while AAIW and UCDW were essential end-members in the thermocline and intermediate layers. We used θ, S, concentrations of O_2, PO_4^{3-}, NO_3^-, and $Si(OH)_4$ data from GEOTRACES GA03 cruise station 3 at ~1000 m to define MW and GEOTRACES GA02 cruise station 9 at ~1000 m to define AAIW and those at ~1500 m to define UCDW (Fig. 1). These end-member properties were in agreement with

511 those reported in literature (Talley et al., 2011; Tsuchiya et al., 1994, refer to Table. 1 for detailed
512 properties).

513 3.2.3 Deep and bottom waters

514 In the west of the section, high O_2, and relatively low NO_3^- and PO_4^{3-} waters are observed from
515 ~1500–4500 m (Figs. 3c, 3e, and 3f). This feature progressively decreases eastwards, but is still
516 visible east of the MAR. It is well established that these distributions are associated with low
517 nutrients and recently ventilated waters from the North Atlantic, mainly leading to the formation
518 of North Atlantic Deep Water: Labrador Sea Water (LSW), North East Atlantic Deep Water
519 (NEADW), and North West Atlantic Bottom Water (NWABW) (Swift, 1984; Talley et al., 2011).
520 LSW is formed in the Labrador Sea by winter convection leading to a homogenous water mass
521 from the surface to a depth of 1500–2000 m depending on the winter severity (Fieux, 2010; Lazier
522 et al., 2002). From the Labrador Sea, LSW is transported in three main directions, including
523 northward in the Irminger Sea, eastward crossing the MAR, and southward within the Deep
524 Western Boundary Current (DWBC, Fieux, 2010; Talley & McCartney, 1982). At 1500 m, the
525 LPTE results show two main flows that transport LSW to the JC150 section (Figs. 4k and 4l): west
526 of the MAR from the Labrador basin within the DWBC, and east of the MAR from the Iceland
527 basin. The first path within the DWBC has been well documented (Fieux, 2010; Talley et al., 2011;
528 Talley & McCartney, 1982). The presence of LSW in the eastern North Atlantic (the eastern
529 subpolar gyre, Iceland Basin, and the Rockall Trough) has also been well documented (Talley et
530 al., 2011). However, we could not find previous works presenting an evidence of the second LSW
531 pathway, east of the MAR and below 40 °N, from the eastern North Atlantic to the eastern tropical
532 Atlantic.
533

Below the LSW layer, NEADW is formed by the mixing of dense Iceland-Scotland Overflow Water (ISOW) with southern origin Lower Deep Water (modified Antarctic Bottom Water), entrained LSW, and subpolar mode water (Lacan & Jeandel, 2005; McCartney, 1992; Read, 2001). NEADW flows in the recirculation cells in the western and eastern parts of the Subpolar North Atlantic Gyre, which are connected to each other through the Charlie-Gibbs Fracture Zone (van Aken, 2007; Fieux, 2010; McCartney & Talley, 1984; Read, 2001; Swift, 1984; Talley et al., 2011). This water mass is known to be transported southward within the DWBC and east of the MAR (Fieux, 2010). The LPTE results (at 2500 m, Figs. 4m and 4n) confirm both pathways.

NWABW is the densest water found near the bottom of the northwest Atlantic (Swift, 1984). It originates from the dense, cold, and ventilated Denmark Strait Overflow Water (DSOW) which, descending over the East Greenland continental slope to the bottom of the North Atlantic Subpolar gyre, mixes with Irminger water, LSW, and ISOW (Fieux, 2010). Contrary to LSW and NEADW, NWABW is too deep to cross the MAR and is therefore restricted to the western basin of the North Atlantic Subpolar Gyre. From there, NWABW flows equatorward within the DWBC along the western margin of the North Atlantic (Fieux, 2010). At 3000 m (data not shown) and 4000 m (Figs. 4o and 4p), the LPTE results confirm the NWABW transport from the Labrador Sea in the DWBC.

The above discussion confirms that LSW, NEADW, and NWABW, which are the main contributors along with the MW to the North Atlantic Deep Water, should be considered as end-members for the JC150 section. The contribution of LSW is specifically required to explain the cold and slightly saline waters of the intermediate layer as well as the warm and low salinity waters of the deep layer (Fig. 2). Therefore, LSW was included in both intermediate and deep layers. LSW, NEADW, and NWABW are needed to explain the $Si(OH)_4$, PO, and NO values at low salinity of the deep layer (Figs. 2b–2d). Therefore, NEADW and NWABW were included in the

deep layer. We used θ, S, concentrations of O_2, PO_4^{3-}, NO_3^-, and $Si(OH)_4$ data from the GEOTRACES GA02 cruise station 9 at ~1000 m to define LSW, ~2500 m to define NEADW, and ~4000 m to define NWABW (Fig. 1). These chosen end-member properties are in agreement with those reported in literature (van Aken, 2007, refer to Table. 1 for detailed properties; Fieux, 2010). A marked increase in the $Si(OH)_4$ concentration is observed in the range of 2500 m to the bottom, which attains a maximum value (> 60 µmol kg^{-1}) in the west of the MAR. This feature reflects the influence of Antarctic Bottom Water (AABW) originating from the Weddell Sea with a $Si(OH)_4$ maximum that can be traced to the North Atlantic (Word Ocean Atlas 2018). Its characteristics and northward expansion are influenced by its mixing with overlying water masses and the complex topography (van Aken, 2007; McCartney, 1992; Talley et al., 2011). AABW is the only water mass that can explain the coldest waters as well as the highest $Si(OH)_4$, NO, and PO waters of the deep layer (Fig. 2). The presence of this water mass in the deep layer is indisputable and was therefore included. We used θ, S, concentrations of O_2, PO_4^{3-}, NO_3^-, and $Si(OH)_4$ data from the GEOTRACES GA02 cruise station 13 at ~4900 m to define AABW (Fig. 1). These chosen end-member properties are in agreement with those reported in literature (van Aken, 2007; McCartney, 1992; Talley et al., 2011).

In summary, the eOMPA thermocline layer includes WNACW, 13 °C-ESACW, AAIW, UCDW, and MW. The eOMPA intermediate layer includes 13 °C-ESACW, AAIW, UCDW, MW, and LSW. The eOMPA deep layer includes MW, LSW, NEADW, NWABW, and AABW. These end-member properties are summarized in Table. 1.

3.3 eOMPA

The eOMPA MATLAB routine was executed with the section data, end-members, weightings, and the Redfield ratios determined earlier. The results from the eOMPA are presented in Figure 5 as sections of end-member contributions. These results are discussed in detail in this section.

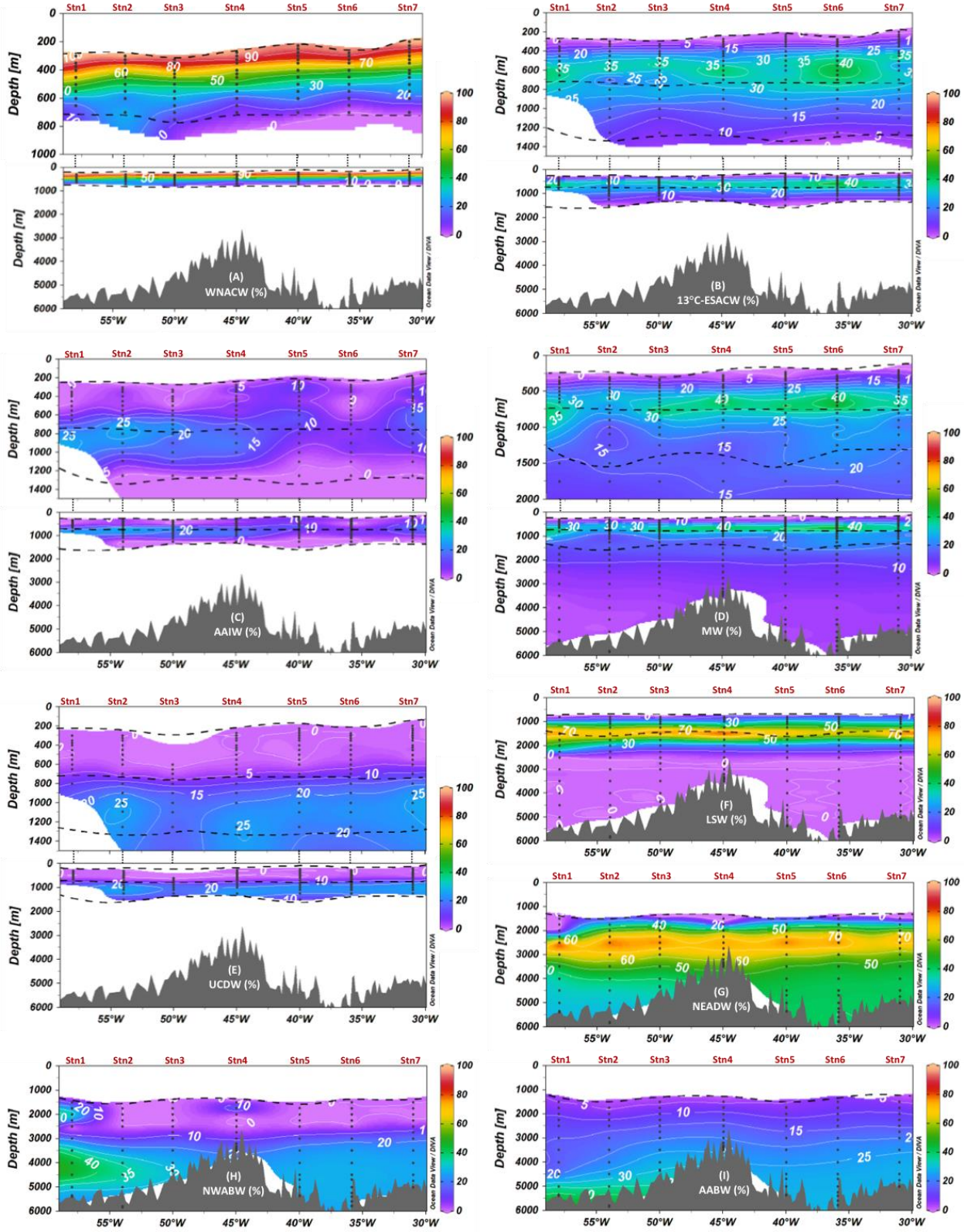
Stn1 Stn2 Stn3 Stn4 Stn5 Stn6 Stn7
Depth [m]
(A) WNACW (%)
(B) 13°C-ESACW (%)
(C) AAIW (%)
(D) MW (%)
(E) UCDW (%)
(F) LSW (%)
(G) NEADW (%)
(H) NWABW (%)
(I) AABW (%)
55°W 50°W 45°W 40°W 35°W 30°W
Ocean Data View / DIVA

583

Fig. 5. Contributions (%) of the different end-members to the JC150 section according to the extended optimum multiparameter analysis (eOMPA) of West North Atlantic Central Water (WNACW) (A), 13°C- East South Atlantic Central Water (ESACW) (B), Antarctic Intermediate Water (AAIW) (C), Mediterranean Water (MW) (D), Upper Circumpolar Deep Water (UCDW) (E), Labrador Sea Water (LSW) (F), North East Atlantic Deep Water (NEADW) (G), North West Atlantic Bottom Water (NWABW) (H), and Antarctic Bottom Water (AABW) (I). Sampling points and eOMPA layer boundaries are represented by black dots and horizontal black dashed lines, respectively.

3.3.1 Residuals and perturbation tests

The validity of the eOMPA results is discussed in this section. Firstly, to verify that the eOMPA reproduces the observed values well, the residuals were closely observed. This aided in determining whether the end-members were accurately selected. Secondly, to evaluate whether the eOMPA results were robust, we discuss the results of the perturbation analysis. This aids in quantifying the sensitivity of the results to our initial choices.

The residuals are presented as sections in Figure S4. The residual values are similar for the three eOMPA layers and their average values are as follows: ~0% for θ, < 1% for S, < 7% for PO, < 9% for NO, < 5% for Si, and ~0% for mass conservation. These average values include one outlier at 1500 m (over 199 samples, station 5). Except for this sample, that does not change the features of the results, the low residue values indicate that the eOMPA well reproduces the observed values. This a posteriori validates the initial choices about the end-members and Redfield ratios.

The results of the three perturbation tests (end-member characteristics, JC150 section data, and parameters weights) enable us to assign an uncertainty/variability (two standard deviation) to each

606 water mass contribution (the section mean values of these uncertainties are reported in Table. S5
607 and presented on sections in Figs. S6, S7, and S8). Overall, the perturbation of both the end-
608 members' properties and the JC150 data result in uncertainties/variabilities of approximately 8%
609 each on average on the water mass percentage results (mean standard deviation over the three
610 eOMPA layers, 2 SD, %). The perturbation of the weights attributed to the eOMPA properties
611 only perturbs the water mass percentage results up to 2% (mean standard deviation over the three
612 eOMPA layers, 2SD, %). Overall, these perturbation analyses show that the main results of the
613 OMPA are robust, i.e., the water mass spatial distribution and their main characteristics (such as
614 dominant water masses) remain unchanged.

615 3.3.2 Thermocline waters

616 WNACW strongly dominates the thermocline layer (Fig. 5a) with a contribution exceeding 90%
617 at ~300 m. This contribution quickly decreases with depth and declines to 50% between 400–500
618 m and under 10% at the depth of ~700 m. The presence of WNACW extends marginally deeper
619 in the west of the section (~100 m deeper than in the east), which is consistent with a stronger
620 WNACW penetration closer to its formation area in the Sargasso Sea (Fieux, 2010; Tomczak &
621 Godfrey, 1994). The dominance of WNACW in this layer was expected based on the two previous
622 basin scale **e**OMPA studies conducted in the Atlantic Ocean thermocline (Poole & Tomczak,
623 1999) and along the GA03 2011 GEOTRACES section (Jenkins et al., 2015) located close to the
624 JC150 section (refer to Fig. 1). Both studies obtained large NACW contributions at depths above
625 600/800 m and the latitude of JC150. The dominance of WNACW in the thermocline layer is also
626 consistent with the LPTE results, indicating that the density of particles coming from the North
627 Atlantic Subtropical Gyre is dominant in the range of 300–600 m (Figs. 4e–4h).

Below the WNACW, a core of 13 °C-ESACW is found across the section with contributions higher than ~30 % in the range of 500–800 m, which attains the maximum at ~600 m depth (35%, Fig. 5b). This result remarkably agrees with a previous eOMPA that estimates a contribution of ~25% at 22 °N:25 °W in the range 400–800 m (Poole & Tomczak, 1999). Below 850 m, the 13 °C-ESACW contribution decreases with depth to under 10 % at ~1250 m. No previous eOMPA study included 13 °C-ESACW as an end-member deeper than 800 m in the Atlantic. However, no other water mass could explain the warm, low salinity, and low PO and NO waters observed in the intermediate layer of the JC150 section (Fig. 3).

3.3.3 Intermediate waters

AAIW is present at depths of 550–1100 m, thereby contributing to both thermocline and intermediate layers. Its contribution is higher west of the MAR, where it attains a maximum at ~700 m (> 30%) (Fig. 5c). UCDW is present over a similar depth range of 700–1500 m just below the AAIW and attains a maximum (> 25 %) at ~1000 m depth. The presence of AAIW and, just below, UCDW in the subtropical Atlantic is consistent with what was reported in previous hydrodynamic studies (Talley et al., 2011; Tsuchiya, 1989; Tsuchiya et al., 1994). This is also supported by two other OMPA studies reporting an AAIW contribution at ~750–900 m immediately above UCDW (Álvarez et al., 2014; Jenkins et al., 2015).

The MW contribution exceeds 25% in the depth range of 500–1000 m across the section with a maximum contribution (> 40 %) centered at ~700 m depth (Fig. 5d). The MW contribution is higher and deeper in the east of the MAR (> 20 % at 1500 m) than in the west of the MAR (> 20 % at ~1000 m), suggesting a westward expansion of this water mass, which is consistent with the MW propagation in the North Atlantic (Fieux, 2010). The MW contribution results are also

comparable with the GA03 OMPA study (Jenkins et al., 2015), according to which the MW contribution extended westward across the MAR at approximately 500–1000 m depth. However, our MW contributions are larger than those reported in other OMPA analyses (Bashmachnikov et al., 2015; Louarn & Morin, 2011). This might be explained by the fact that our MW end-member was defined further away from the Strait of Gibraltar and included a contribution of subsurface and intermediate waters of the Northeast Atlantic (refer to section 3.2.2). The MW maximum contribution is in the same depth range as that of AAIW; however, MW is more pronounced in the east, whereas AAIW is more pronounced in the west. This is consistent with the mixing of MW with AAIW at approximately 20 °N (Fieux, 2010; Talley et al., 2011). In the deep eOMPA layer, the MW contribution is under 10% deeper than 2300 m and under 5% deeper than 3500 m. This is consistent with the GA03 OMPA study that reported an MW contribution of ~10% in the range of 2000–3600 m (Jenkins et al., 2015). Though this contribution in our deep layer eOMPA is low, it is not zero. It is absolutely necessary to account for the deep layer saltiest waters (refer to the red triangle in Fig. 2a), which is in agreement with initial findings of Reid et al. (1979).

3.3.4 Deep waters

LSW is included in both intermediate and deep eOMPA layers. This water mass is present across the section and exceeds a contribution of over 20% in the depth range of 900–2000 m. Its contribution exceeds 50% in the depth range of 1250–1750 m and attains a maximum (> 70 %) at ~1500 m depth (Fig. 5f). This is consistent with the GA01 (Subpolar Gyre) eOMPA study, that found LSW centered at 1500 m in the Iceland and west European Basins (García-Ibáñez et al., 2018). It is also consistent with the GA03 OMPA study that found the Upper LSW centered at 1500 m across the MAR (Jenkins et al., 2015).

672 The NEADW contribution exceeds 30% from ~2000 m to the bottom across the section (Fig. 5g).
673 Its maximum (>70 %) is attained at ~2500 m. The NEADW contribution is under 40% at a depth
674 of over 4000 m and in the west of the MAR, while the contribution in the east of the MAR is over
675 40% down to the bottom. This is consistent with the LPTE results and previous studies that suggest
676 that the NEADW contribution is achieved not only from the DWBC, but also directly from the
677 eastern part of the Subpolar North Atlantic Gyre east of the MAR (van Aken, 2007; Fieux, 2010;
678 McCartney, 1992; Read, 2001; Talley et al., 2011).

679 Below the NEADW, NWABW appears from 3000 m (> 10 %) to the bottom and attains its
680 maximum (> 45 %) at approximately 4000–4500 m at the section's western end (Fig. 5h). This
681 maximum seems to expand eastward to the MAR. East of the MAR, the NWABW contribution
682 exceeds 25% from 4000 m to the bottom. Four data points located shallower than 2500 m present
683 an unrealistic high NWABW contribution of over 19% and are clear outliers (Station 1 1750 m,
684 2000 m, and 2251 m and Station 4 1750 m), as a previous work has reported that this water mass
685 is absent at such shallow depths (García-Ibáñez et al., 2018). The lack of continuity between the
686 calculated NWABW core (observed here at 4000–4500 m) and these points is also an argument
687 for excluding these four data points. These four outliers should correspond to a predominance of
688 LSW and NEADW. LSW, NEADW, and NWABW have very close properties (almost
689 undistinguishable in terms of S, PO, NO, and $Si(OH)_4$ and temperature differences in the order of
690 1 °C, refer to Fig. 2). These similitudes explain that the deep eOMPA did not accurately distinguish
691 the three end-members for these four outliers. However, for the other 84 data points of the deep
692 layer (88 data points in total), the eOMPA appropriately distinguished between LSW, NEADW,
693 and NWABW and provided results, which are consistent with the literature (notably LSW above
694 NEADW above NWABW, Lacan & Jeandel, 2005; Swift, 1984). The maximum NWABW

contribution in the west is consistent with what was reported in previous studies on NWABW flowing equatorward from the Labrador basin with DWBC along the western margin of the North Atlantic (Fieux, 2010). However, the significant NWABW contribution east of the MAR (up to ~ 20%) is unexpected or at least unreported so far. This water mass, which is formed in the Labrador and Irminger Basins, is too dense to cross the MAR through the Charlie-Gibbs Fracture Zone and was therefore never observed east of the MAR in the North Atlantic Subpolar Gyre. Flowing southward from there, the first passage sufficiently deep for the NWABW to cross the MAR is the Kane fracture zone, which is localized at 24 °N (just north of the JC150 section at 22 °N, Fig. 1) with a sill depth of ~4350 m (Morozov et al., 2017). The next passage that is sufficiently deep is the Vema Fracture Zone with a sill depth of ~5000 m; however, it is located much further south (10–11 °N, Kastens et al., 1998). Therefore, our results suggest that NWABW enters the eastern Atlantic through the Kane fracture zone. This eastern trajectory is confirmed by the LPTE results, which indicates particles originating directly from the eastern part of the Subpolar North Atlantic Gyre east of the MAR at 4000 m (Fig. 4p). We could not find any previous study describing this aspect.

Note that our results about the localization of NEADW above NWABW contradicts with those of the GA03 OMPA, which found DSOW (that significantly contributes to the formation of NWABW) lying above ISOW (that significantly contributes to the formation of NEADW) (Jenkins et al., 2015). Our results confirm that NWABW (including DSOW) lies below NEADW (including ISOW) in the subtropical North Atlantic. In addition, our results are consistent in terms of the densities of NWABW and DSOW being higher than those of NEADW and ISOW, respectively. It is generally consistent with the current understanding of deep water mass dynamics in the North Atlantic as well (Fieux, 2010; Lacan & Jeandel, 2005; Middag et al., 2015; Swift,

718 1984).

719 Deeper than 3000 m, the AABW contribution exceeds 15% across the section. West of the MAR,
720 AABW attains its maximum contribution (> 35%) from 5000 m to the bottom. East of the MAR,
721 the AABW contribution stays relatively high (> 20%) at a depth of over 3500 m. This AABW
722 contribution to bottom waters of the section and across the MAR is consistent with the findings
723 reported in previous studies, which describe AABW as the densest water in the majority of the
724 Atlantic, moving northward from its formation zone and crossing the MAR at 11 °N through the
725 Vema fracture zone (van Aken, 2007; McCartney, 1992; Talley et al., 2011). This AABW
726 contribution is also consistent with the GA03 OMPA study, in which a contribution of AABW is
727 observed across the MAR in the deepest parts of both the western and eastern basins (Jenkins et
728 al., 2015).

729

730 **4 Conclusions**

731 Based on i) the hydrographic data (θ, S, concentrations of O_2, NO_3^-, PO_4^{3-}, and $Si(OH)_4$), ii) an
732 eOMPA, and iii) an LPTE conducted in an eddy-resolving ocean circulation model, a water mass
733 analysis has been presented for the 2017 JC150 GEOTRACES process study (GApr08) in the
734 subtropical North Atlantic along 22 °N.
735 This is the first time to the best of our knowledge that a water mass analysis combined an eOMPA
736 with an LPTE. This approach demonstrated several advantages:
737 - In addition to a thorough literature review and a meticulous analysis of the hydrographic data,
738 the LPTE helped select the eOMPA end-members. This is important, because the eOMPA results
739 are very sensitive to end-member choice. This meticulous end-member's choice enabled the

eOMPA to reproduce the observations (small residuals) and provide results, which were in good agreement with the current knowledge (notably other Atlantic OMPA studies).

- LPTE provided information about water mass trajectories between their formation areas and the studied location, which could not be achieved with a sole eOMPA.
- Finally, LPTE was effective in tracing water mass origins in surface layers, where an eOMPA could not be performed due to the non-conservative hydrographic parameters.

The following conclusions were drawn from our study. The upper 100 m is occupied by a shallow type of ESACW with impacts of the Amazon River plume in the west of the section. The WNACW contribution dominates the upper part of the transect (mainly between 100–500 m) with a contribution exceeding 90% at approximately 300 m. The 13 °C-ESACW contribution appears marginally deeper with a contribution exceeding 40% at approximately 600 m depth. The AAIW presents a maximum contribution of over 30% in the west of the MAR at ~700 m. At approximately the same depth, MW, whose high salinity signal is lost because of mixing with AAIW, attains its maximum contribution of over 40% in the east of the MAR. We found that MW's contribution, although in small quantities (in the order of 5%), is required down to 3500 m. Just below AAIW, the UCDW maximum contribution of over 25% is observed at ~1000 m depth. The LSW contribution is present in the depth of 900–2000 m with a maximum of over 70% at ~1500 m depth all across the section. Unpredictably, at this depth, we found through the LPTE that the LSW present in the eastern North Atlantic flows southward to the eastern subtropical Atlantic. We could not find previous works presenting this evidence below 40 °N. Below LSW, the NEADW contribution, which includes the ISOW contribution, exceeds 70% at approximately 2500 m all across the section. Below NEADW, the NWABW maximum contribution of over 45% is attained at ~4500 m west of the MAR. The NWABW contribution is also found in the east of

763 the MAR in significant proportions (> 25 %). Crossing of the MAR by this water mass has not
764 been investigated so far. As this water is too dense to cross the MAR in the Subpolar Gyre (through
765 the Charlie-Gibbs Fracture Zone), we suggest that it crosses the MAR through the Kane fracture
766 zone (sill depth of 4350 m) at ~24 °N. The occurrence of NWABW (including DSOW) below
767 NEADW (including ISOW) is consistent with the current knowledge about these water masses
768 and notably their densities. This contradicts a recent OMPA result obtained in a nearby area, where
769 ISOW was found below DSOW (GA03, Jenkins et al., 2015). The deeper water mass contributing
770 to our section is AABW with a maximum contribution of over 35% deeper than 5000 m in the
771 west of the MAR.

772 These results will be useful to interpret the biogeochemical datasets from the subtropical North
773 Atlantic, notably those with respect to trace elements and isotope distributions (which can be
774 facilitated by the end-member choices at GEOTRACES stations).

775

776 **Author contributions**

777 CM was the chief scientist of the cruise. CM, MCL, NJW, and EMSW participated in the sampling
778 on board. They participated in the temperature, salinity, dissolved oxygen, and nutrient
779 concentration data production along with JH. SvG produced the Lagrangian particle tracking
780 experiment under the supervision of YD with the contribution of LA and FL. LA and FL produced
781 the optimum multiparameter analysis and conducted the interpretation work. LA drafted the
782 manuscript under the supervision of FL with contributions from SvG, NJW, and all other authors.

Acknowledgments

We dedicate this work to Pr. Matthias Tomczack for his invaluable contributions to the Oceanographic community. As part of his large body of work, Matthias Tomczack introduced and developed the optimum multiparameter analysis. We particularly thank him for his thoughtful answers to our questions and his helpful explanations of his work.

We sincerely thank Dr. Johannes Karstensen for providing the OMP Analysis Package for MATLAB Version 2.0 with a clear manual of utilization on the website: https://omp.geomar.de/

We sincerely thank Dr. Gael Alory for providing the July 2017 salinity map from the SMOS satellite and Dr. Julien Jouanno for his helpful comments on the Amazon River plume. We thank Dr. Elodie Kestenar and Manon Gevaudan for their help with MATLAB.

Last, but not the least, we would like to thank the captain and crew of RRS James Cook for their help at sea as well as all of the scientists involved in JC150.

References

van Aken, H. M. van. (2007). *The oceanic thermohaline circulation: an introduction*. New York: Springer.

Álvarez, M., Brea, S., Mercier, H., & Álvarez-Salgado, X. A. (2014). Mineralization of biogenic materials in the water masses of the South Atlantic Ocean. I: Assessment and results of an optimum multiparameter analysis. *Progress in Oceanography*, *123*, 1–23. https://doi.org/10.1016/j.pocean.2013.12.007

Amante, C., & Eakins, B. W. (2009). ETOPO1 1 Arc-minute global relief model: procedures, data sources and analysis. *NOAA Technical Memorandum NESDIS NGDC-24, Marine Geology and Geophysics Division, Boulder, Colorado*, 25.

Anderson, L. A. (1995). On the hydrogen and oxygen content of marine phytoplankton. *Deep Sea Research Part I: Oceanographic Research Papers*, *42*(9), 1675–1680. https://doi.org/10.1016/0967-0637(95)00072-E

Anderson, L. A., & Sarmiento, J. L. (1994). Redfield ratios of remineralization determined by nutrient data analysis. *Global Biogeochemical Cycles*, *8*(1), 65–80. https://doi.org/10.1029/93GB03318

Baringer, M. O. (1997). Mixing and Spreading of the Mediterranean Outflow. *Journal of Physical Oceanography*, *27*, 24.

Bashmachnikov, I., Nascimento, Â., Neves, F., Menezes, T., & Koldunov, N. V. (2015). Distribution of intermediate water masses in the subtropical northeast Atlantic. *Ocean Science*, *11*(5), 803–827. https://doi.org/10.5194/os-11-803-2015

Becker, J. J., Sandwell, D. T., Smith, W. H. F., Braud, J., Binder, B., Depner, J., et al. (2009). Global Bathymetry and Elevation Data at 30 Arc Seconds Resolution: SRTM30_PLUS. *Marine Geodesy*, *32*(4), 355–371. https://doi.org/10.1080/01490410903297766

Blanke, B., & Raynaud, S. (1997). Kinematics of the Pacific Equatorial Undercurrent: An Eulerian and Lagrangian Approach from GCM Results. *Journal of Physical Oceanography*, *27*(6), 1038–1053. https://doi.org/10.1175/1520-0485(1997)027<1038:KOTPEU>2.0.CO;2

Boyle, E. A., Anderson, R. F., Cutter, G. A., Fine, R., Jenkins, W. J., & Saito, M. (2015). GEOTRACES GA-03 - The U.S. GEOTRACES North Atlantic Transect. *Deep Sea Research Part II: Topical Studies in Oceanography*, *116*, 1–342.

Broecker, W. S. (1974). "NO", a conservative water-mass tracer. *Earth and Planetary Science Letters*, *23*(1), 100–107. https://doi.org/10.1016/0012-821X(74)90036-3

Broecker, W. S., Takahashi, T., & Takahashi, T. (1985). Sources and flow patterns of deep-ocean waters as deduced from potential temperature, salinity, and initial phosphate concentration. *Journal of Geophysical Research*, *90*(C4), 6925. https://doi.org/10.1029/JC090iC04p06925

Broecker, W. S., Blanton, S., Smethie, W. M., & Ostlund, G. (1991). Radiocarbon decay and oxygen utilization in the Deep Atlantic Ocean. *Global Biogeochemical Cycles*, *5*(1), 87–117. https://doi.org/10.1029/90GB02279

Browning, T. J., Achterberg, E. P., Yong, J. C., Rapp, I., Utermann, C., Engel, A., & Moore, C. M. (2017). Iron limitation of microbial phosphorus acquisition in the tropical North Atlantic. *Nature Communications*, *8*. https://doi.org/10.1038/ncomms15465

Carracedo, L. I., Pardo, P. C., Flecha, S., & Pérez, F. F. (2016). On the Mediterranean Water Composition. *Journal of Physical Oceanography*, *46*(4), 1339–1358. https://doi.org/10.1175/JPO-D-15-0095.1

Cetina-Heredia, P., van Sebille, E., Matear, R., & Roughan, M. (2016). Lagrangian characterization of nitrate supply and episodes of extreme phytoplankton blooms in the Great Australian Bight. *Biogeosciences Discussions*, 1–15. https://doi.org/10.5194/bg-2016-53

Fieux, M. (2010). *L'océan planétaire*. Les Presses de l'ENSTA.

García-Ibáñez, M. I., Pérez, F. F., Lherminier, P., Zunino, P., Mercier, H., & Tréguer, P. (2018). Water mass distributions and transports for the 2014 GEOVIDE cruise in the North Atlantic. *Biogeosciences*, *15*(7), 2075–2090. https://doi.org/10.5194/bg-15-2075-2018

Harvey, J. (1982). θ-S relationships and water masses in the eastern North Atlantic. *Deep Sea Research Part A. Oceanographic Research Papers*, *29*(8), 1021–1033. https://doi.org/10.1016/0198-0149(82)90025-5

Hinrichsen, H.-H., & Tomczak, M. (1993). Optimum multiparameter analysis of the water mass structure in the western North Atlantic Ocean. *Journal of Geophysical Research: Oceans*, *98*(C6), 10155–10169. https://doi.org/10.1029/93JC00180

Holte, J., Talley, L. D., Gilson, J., & Roemmich, D. (2017). An Argo mixed layer climatology and database: ARGO MLD CLIMATOLOGY. *Geophysical Research Letters*, *44*(11), 5618–5626. https://doi.org/10.1002/2017GL073426

Jenkins, W. J., Smethie, W. M., Boyle, E. A., & Cutter, G. A. (2015). Water mass analysis for the U.S. GEOTRACES (GA03) North Atlantic sections. *Deep Sea Research Part II: Topical Studies in Oceanography*, *116*, 6–20. https://doi.org/10.1016/j.dsr2.2014.11.018

Kastens, K., Bonatti, E., Caress, D., Carrara, G., Dauteuil, O., Frueh-Green, G., et al. (1998). The Vema Transverse Ridge (Central Atlantic), 2.
Kim, I.-N., Min, D.-H., & Macdonald, A. M. (2013). Water column denitrification rates in the oxygen minimum layer of the Pacific Ocean along 32°S. *Global Biogeochemical Cycles*, *27*(3), 816–827. https://doi.org/10.1002/gbc.20070
Lacan, F., & Jeandel, C. (2005). Acquisition of the neodymium isotopic composition of the North Atlantic Deep Water. *Geochemistry, Geophysics, Geosystems*, *6*(12), n/a-n/a. https://doi.org/10.1029/2005GC000956
Lazier, J., Hendry, R., Clarke, A., Yashayaev, I., & Rhines, P. (2002). Convection and restratification in the Labrador Sea, 1990–2000. *Deep Sea Research Part I: Oceanographic Research Papers*, *49*(10), 1819–1835. https://doi.org/10.1016/S0967-0637(02)00064-X
Lellouche, J.-M., Le Galloudec, O., Greiner, E., Garric, G., Régnier, C., Clavier, M., et al. (2018b). Performance and quality assessment of the current Copernicus Marine Service global ocean monitoring and forecasting real-time system. In *Operational Oceanography serving Sustainable Marine Development.* (pp. 251–260). EuroGOOS. Brussels, Belgium.
Lellouche, J.-M., Greiner, E., Le Galloudec, O., Garric, G., Regnier, C., Drevillon, M., et al. (2018a). Recent updates to the Copernicus Marine Service global ocean monitoring and forecasting real-time 1⁄12° high-resolution system. *Ocean Science*, *14*(5), 1093–1126. https://doi.org/10.5194/os-14-1093-2018
Louarn, E., & Morin, P. (2011). Antarctic Intermediate Water influence on Mediterranean Sea Water outflow. *Deep Sea Research Part I: Oceanographic Research Papers*, *58*(9), 932–942. https://doi.org/10.1016/j.dsr.2011.05.009
Mackas, D. L., Denman, K. L., & Bennett, A. F. (1987). Least squares multiple tracer analysis of water mass composition. *Journal of Geophysical Research*, *92*(C3), 2907. https://doi.org/10.1029/JC092iC03p02907
Madec, G., & the NEMO team. (2008). NEMO ocean engine, Note du Pôle de modélisation. *Institut Pierre-Simon Laplace (IPSL)*, pp. 1288–1619.
Mahaffey, C., Reynolds, S., Davis, C. E., & Lohan, M. C. (2014). Alkaline phosphatase activity in the subtropical ocean: insights from nutrient, dust and trace metal addition experiments. *Frontiers in Marine Science*, *1*. https://doi.org/10.3389/fmars.2014.00073
McCartney, M. S. (1992). Recirculating components to the deep boundary current of the northern North Atlantic. *Progress in Oceanography*, *29*(4), 283–383. https://doi.org/10.1016/0079-6611(92)90006-L
McCartney, M. S., & Talley, L. D. (1984). Warm-to-Cold Water Conversion in the Northern North Atlantic Ocean. *Journal of Physical Oceanography*, *14*(5), 922–935. https://doi.org/10.1175/1520-0485(1984)014<0922:WTCWCI>2.0.CO;2
Middag, R., van Hulten, M. M. P., Van Aken, H. M., Rijkenberg, M. J. A., Gerringa, L. J. A., Laan, P., & de Baar, H. J. W. (2015). Dissolved aluminium in the ocean conveyor of the West Atlantic Ocean: Effects of the biological cycle, scavenging, sediment resuspension and hydrography. *Marine Chemistry*, *177*, 69–86. https://doi.org/10.1016/j.marchem.2015.02.015
Moore, C. M., Mills, M. M., Achterberg, E. P., Geider, R. J., LaRoche, J., Lucas, M., et al. (2009). Large-scale distribution of Atlantic nitrogen fixation controlled by iron availability. https://doi.org/10.1038/NGEO667
Morozov, E. G., Tarakanov, R. Yu., Demidova, T. A., & Makarenko, N. I. (2017). Flows of bottom water in fractures of the North Mid-Atlantic Ridge. *Doklady Earth Sciences*, *474*(2), 653–656. https://doi.org/10.1134/S1028334X17060058

Pardo, P. C., Pérez, F. F., Velo, A., & Gilcoto, M. (2012). Water masses distribution in the Southern Ocean: Improvement of an extended OMP (eOMP) analysis. *Progress in Oceanography*, *103*, 92–105. https://doi.org/10.1016/j.pocean.2012.06.002

Peters, B. D., Jenkins, W. J., Swift, J. H., German, C. R., Moffett, J. W., Cutter, G. A., et al. (2018). Water mass analysis of the 2013 US GEOTRACES eastern Pacific zonal transect (GP16). *Marine Chemistry*, *201*, 6–19. https://doi.org/10.1016/j.marchem.2017.09.007

Poole, R., & Tomczak, M. (1999). Optimum multiparameter analysis of the water mass structure in the Atlantic Ocean thermocline. *Deep Sea Research Part I: Oceanographic Research Papers*, *46*(11), 1895–1921. https://doi.org/10.1016/S0967-0637(99)00025-4

Read, J. F. (2001). CONVEX-91: water masses and circulation of the Northeast Atlantic subpolar gyre. *Progress in Oceanography*, *48*(4), 461–510. https://doi.org/10.1016/S0079-6611(01)00011-8

Reid, J. L. (1979). On the contribution of the Mediterranean Sea outflow to the Norwegian-Greenland Sea. *Deep Sea Research Part A. Oceanographic Research Papers*, *26*(11), 1199–1223. https://doi.org/10.1016/0198-0149(79)90064-5

Rijkenberg, M. J. A., Middag, R., Laan, P., Gerringa, L. J. A., van Aken, H. M., Schoemann, V., et al. (2014). The Distribution of Dissolved Iron in the West Atlantic Ocean. *PLOS ONE*, *9*(6), e101323. https://doi.org/10.1371/journal.pone.0101323

Schlitzer, R., Anderson, R. F., Dodas, E. M., Lohan, M., Geibert, W., Tagliabue, A., et al. (2018). The GEOTRACES Intermediate Data Product 2017. *Chemical Geology*, *493*, 210–223. https://doi.org/10.1016/j.chemgeo.2018.05.040

Snow, J. T., Schlosser, C., Woodward, E. M. S., Mills, M. M., Achterberg, E. P., Mahaffey, C., et al. (2015). Environmental controls on the biogeography of diazotrophy and Trichodesmium in the Atlantic Ocean. *Global Biogeochemical Cycles*, *29*(6), 865–884. https://doi.org/10.1002/2015GB005090

Spence, P., van Sebille, E., Saenko, O. A., & England, M. H. (2014). Using Eulerian and Lagrangian Approaches to Investigate Wind-Driven Changes in the Southern Ocean Abyssal Circulation. *Journal of Physical Oceanography*, *44*(2), 662–675. https://doi.org/10.1175/JPO-D-13-0108.1

Stramma, L., & Schott, F. (1999). The mean flow field of the tropical Atlantic Ocean. *Deep Sea Research Part II: Topical Studies in Oceanography*, *46*(1–2), 279–303. https://doi.org/10.1016/S0967-0645(98)00109-X

Swift, J. H. (1984). The circulation of the Denmark Strait and Iceland-Scotland overflow waters in the North Atlantic. *Deep Sea Research Part A. Oceanographic Research Papers*, *31*(11), 1339–1355. https://doi.org/10.1016/0198-0149(84)90005-0

Talley, L. D. (1996). Antarctic Intermediate Water in the South Atlantic. In *The South Atlantic* (pp. 219–238). Berlin, Heidelberg: Springer Berlin Heidelberg. https://doi.org/10.1007/978-3-642-80353-6

Talley, L. D., & McCartney, M. S. (1982). Distribution and circulation of Labrador Sea Water. *Journal of Physical Oceanography*, *12*, 1189–1205.

Talley, L. D., Pickard, G. L., Emery, W. J., & Swift, J. H. (Eds.). (2011). *Descriptive physical oceanography: an introduction* (6. ed). Amsterdam: Elsevier.

Tomczak, M. (1981). A multi-parameter extension of temperature/salinity diagram techniques for the analysis of non-isopycnal mixing. *Progress in Oceanography*, *10*(3), 147–171. https://doi.org/10.1016/0079-6611(81)90010-0

Tomczak, M. (1999). Some historical, theoretical and applied aspects of quantitative water mass

analysis. *Journal of Marine Research*, *57*(2), 275–303.
https://doi.org/10.1357/002224099321618227
Tomczak, M., & Godfrey, J. S. (1994). Regional-Oceanography-An-Introduction.pdf.
Tomczak, M., & Large, D. G. B. (1989). Optimum multiparameter analysis of mixing in the thermocline of the eastern Indian Ocean. *Journal of Geophysical Research*, *94*(C11), 16141.
https://doi.org/10.1029/JC094iC11p16141
Tsuchiya, M. (1986). Thermostads and Circulation in the Upper Layer of the Atlantic Ocean. *Progress in Oceanography*.
Tsuchiya, M. (1989). Circulation of the Antarctic Intermediate Water in the North Atlantic Ocean. *Journal of Marine Research*, *47*(4), 747–755.
https://doi.org/10.1357/002224089785076136
Tsuchiya, M., Talley, L. D., & McCartney, M. S. (1994). Water-mass distributions in the western South Atlantic; A section from South Georgia Island (54S) northward across the equator. *Journal of Marine Research*, *52*(1), 55–81. https://doi.org/10.1357/0022240943076759
Wu, J., Sunda, W., Boyle, E. A., & Karl, D. M. (2000). Phosphate Depletion in the Western North Atlantic Ocean, *289*, 4.
Zhang, J.-Z., & Chi, J. (2002). Automated Analysis of Nanomolar Concentrations of Phosphate in Natural Waters with Liquid Waveguide. *Environmental Science & Technology*, *36*(5), 1048–1053. https://doi.org/10.1021/es011094v